Anisotropy in magnetic properties and electronic structure of single-crystal $LiFePO_4$

Gan Liang,[1,*] Keeseong Park,[2] Jiying Li,[3] Ronald E. Benson,[4] David Vaknin,[3] John T. Markert,[2] and Mark C. Croft[5]
[1]*Department of Physics, Sam Houston State University, Huntsville, Texas 77341, USA*
[2]*Department of Physics, University of Texas at Austin, Austin, Texas 78712, USA*
[3]*Ames Laboratory and Department of Physics and Astronomy, Iowa State University, Ames, Iowa 50011, USA*
[4]*Rigaku Americas Corporation, 9009 New Trails Drive, The Woodlands, Texas 773801, USA*
[5]*Department of Physics and Astronomy, Rutgers University, Piscataway, New Jersey 08854, USA and NSLS, Brookhaven National Laboratory, Upton, New York 11973, USA*
(Received 4 August 2007; revised manuscript received 19 November 2007; published 12 February 2008)

We report the experimental and theoretical results on the anisotropies in the magnetic properties and x-ray absorption spectra of single-crystal $LiFePO_4$. A mean-field theory is developed to explain the observed strong anisotropies in Lande *g*-factor, paramagnetic Curie temperature, and effective moment for $LiFePO_4$ single crystals. The values of the in-plane nearest- and next-nearest-neighbor spin exchange (J_1 and J_2), interplane spin exchange ($J_\perp$), and single-ion anisotropy (D), obtained recently from neutron scattering measurements, are used for calculating the Curie temperatures with the formulas derived from the mean-field Hamiltonian. It is found that the calculated Curie temperatures match well with that obtained by fitting the magnetic susceptibility curves to the modified Curie-Weiss law. For the polarized Fe *K*-edge x-ray absorption spectra of single-crystal $LiFePO_4$, a different feature assignment for the $1s \rightarrow 4p$ transition features is proposed and the anisotropy in the intensities of the $1s \rightarrow 3d$ transition features is explained adequately by a one-electron theory calculation of the electric quadrupole transition terms in the absorption coefficient.

DOI: 10.1103/PhysRevB.77.064414 PACS number(s): 75.30.Gw, 78.70.Dm, 75.50.Ee, 61.05.cp

I. INTRODUCTION

Lithium iron phosphate ($LiFePO_4$) has been considered to be one of the most promising candidates for next generation Li-ion batteries cathode materials due to its high theoretical specific capacity (~170 mA h/g), high cycle life, low cost, high thermal stability, and nontoxicity.[1–6] However, the intrinsically poor electronic and ionic conductivities of $LiFePO_4$ limit the delivery of high specific capacity at high discharge rates.[3,7–10] The low ionic conductivity can be attributed to the one-dimensional nature of Li diffusion in olivine $LiFePO_4$, as clearly shown by a recent first principles calculation.[9,10] At present, there is a controversy regarding whether the enhancement in the electronic conductivity for cation-doped $LiFePO_4$ is truly due to the substitution of Li^+ by the cations or due to the grain-boundary impurity network.[3,11–14] One of the effective ways to resolve this controversy is to synthesize pure phase and sizable (>10 mm^3, for example) cation-doped $LiFePO_4$ single crystals for electronic conductivity studies, because such single crystals could be free of impurity grain boundaries, and thus the complicating factor due to grain boundaries can be ruled out. Also, the anisotropies of the magnetic and electronic structures can be studied only by using high quality and sizable single crystals. It is important to synthesize large-size and high quality $LiFePO_4$ and cation-doped $LiFePO_4$ single crystals for the study of the electronic conductivity and other physical and/or electrochemical properties.

Currently, due to the unavailability of large-size $LiFePO_4$ single crystals, almost all of the studies including those on electronic conductivity measurements were carried out on polycrystalline $LiFePO_4$-based materials synthesized by various methods.[3,15–21] The crystal structure of $LiFePO_4$ has been studied previously by a number of groups.[22–27] Figure 1(a) is a general view of the structure which contains the distorted FeO_6 octahedra (in blue) and PO_4^{-3} tetrahedra (in yellow). A sketch of such a distorted FeO_6 octahedron is displayed in Fig. 1(c), which will be discussed in detail in Sec. III A below. Each FeO_6 octahedron is connected to four other FeO_6 octahedra in the *bc* plane (determined by the [010] and [001] axes) by corner sharing and four PO_4 tetrahedra, and it has one common edge (along the *b*-axis direction) with a PO_4 tetrahedron and two common edges with a LiO_6 octahedron. The Li ions are located at the inversion centers of highly distorted LiO_6 octahedra, which form an edge sharing chain along the *b*-axis (or [010]) direction. Figure 1(b) shows the spin arrangement of two adjacent Fe^{2+} layers and the three nearest-neighbor (NN) and next-nearest-neighbor (NNN) exchange interactions J_1, J_2, and $J_\perp$ (to be discussed in detail in Sec. III B 2).

In the past, few results on the growth of $LiFePO_4$ single crystals were reported. For example, the hydrothermal growth[20,28] has been reported, but the grown $LiFePO_4$ single crystals were too small (with radius less than 0.15 mm) to be used for certain physical property studies such as the measurements of four-probe electronic conductivity. Recently, growth of $LiFePO_4$ crystals using optical and traveling solvent floating zone techniques were reported.[29,30] In the 1960s, Mercier *et al.*[31–33] reported the growth of single crystals of $LiMPO_4$ (M=Mn, Co, Ni, and Fe) by a flux method, however, the size and quality of the crystals were not reported. To our knowledge, there have been virtually no detailed reports on the growth of sizable pure phase $LiFePO_4$ single crystals using flux method. Very recently, we have successfully grown $LiFePO_4$ single crystals by a flux method for magnetic neutron scattering study.[34] In this paper, we report (1) the details of the growth of sizable and high quality $LiFePO_4$ single crystals by standard flux method and the

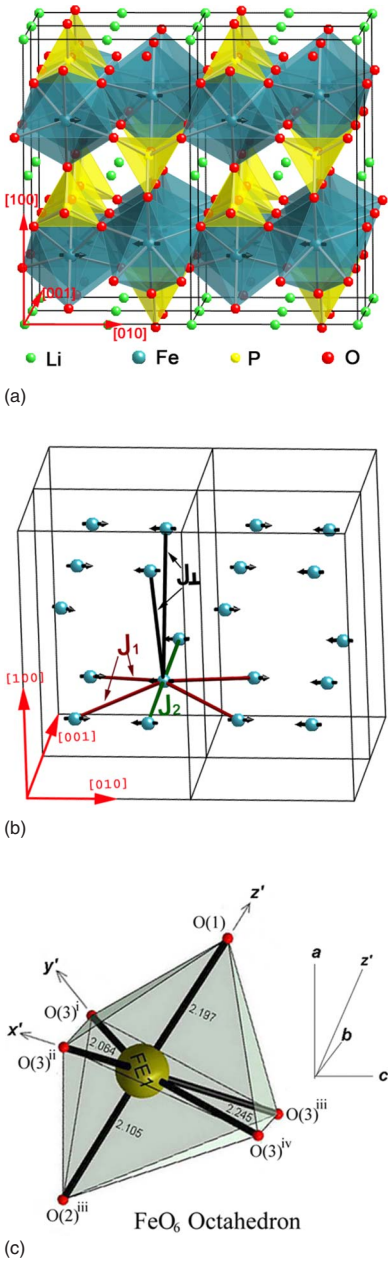

FIG. 1. (Color online) (a) The structure of the orthorhombic $LiFePO_4$ showing atomic positions, as indicated. The blue octahedra represent FeO_6 and the yellow tetrahedra represent PO_4^{3-}. The arrows at the Fe sites represent the spin moments. (b) The arrangement of two adjacent Fe^{2+} spin layers with the three exchange interaction parameters J_1, J_2, and $J_\perp$ labeled. (c) The sketch of a single distorted FeO_6 octahedron with the values of Fe-O bond lengths labeled. The angle between the a axis and z' axis is about 30.2°. The values of the bond lengths and the coordinates of the atoms are listed in Tables I and II.

results on the single-crystal (SC) x-ray diffraction (XRD); (2) the experimental results of magnetic susceptibility and the theoretical study on the observed strong anisotropies in g-factor, paramagnetic Curie temperature, and effective moment for $LiFePO_4$ single crystals; and (3) the polarized Fe K-edge x-ray absorption spectroscopy (XAS) study on single-crystal $LiFePO_4$ (note that XAS studies on polycrystalline $LiFePO_4$ samples were carried out previously by other groups), with a different assignment for the $1s \rightarrow 4p$ transition features and a one-electron theoretical explanation of the observed anisotropy in the intensities of the $1s \rightarrow 3d$ transition features.

II. EXPERIMENTAL DETAILS

$LiFePO_4$ single crystals were grown by a standard flux growing technique from stoichiometric mixture of high purity $FeCl_2$ (99.999% Aldrich) and Li_3PO_4 (99.999% Aldrich), carried out in an Ar atmosphere. LiCl was used as the flux during the following chemical reaction: $FeCl_2+Li_3PO_4+LiCl=LiFePO_4+3LiCl$. The crystals were extracted from the flux mixture by dissolving the extra LiCl by water at room temperature. The procedure of the crystal growth was essentially the same as that used by Formin *et al.*[35] for the growth of $LiNiPO_4$.

The SC XRD data were measured at $T=293$ K using a Rigaku SPIDER x-ray diffractometer with Mo $K\alpha$ radiation ($\lambda=0.7107$ Å) to a resolution corresponding to $\sin\theta_{max}/\lambda \approx 0.65$ Å^{-1}. The data refinement was done using the program SHELXL.[36] Powder XRD of ground single crystals at room temperature was measured on a Rigaku Geigerflex diffractometer using Cu $K\alpha$ radiation with wavelength of 1.5406 Å. The intensity data were accumulated at 0.02° step and a scanning rate of 5 s/step. The data were analyzed by the software package JADE 6.1 provided by Material Data Inc. The temperature and field dependent magnetic susceptibility measurements were carried out on a commercial superconducting quantum interference device magnetometer (model MPMS, Quantum Design) in a temperature range from 5 to 300 K and magnetic fields up to 5 T. The Fe K-edge XAS data were taken at room temperature and in fluorescence at beamline X-19A of the National Synchrotron Light Source. A double-crystal Si (111) monochromator was used for energy selection. At the Fe K edge, the monochromator was detuned by reducing the incident photon flux by about 20% in order to suppress contamination from harmonics. The energy resolution ($\Delta E/E$) of the X-19A beamline was 2×10^{-4}, corresponding to about 1.4 eV at the Fe K edge. For energy calibration, after measuring each spectrum of the single crystal, an FeO powder reference sample was measured together with the single crystal. All of the XAS spectra presented in this paper were background subtracted and normalized to unity in the continuum region.

III. RESULTS AND DISCUSSION

A. Single-crystal x-ray diffraction

The as-grown single crystals have an average size of $4\times4\times6$ mm$^3 \approx 100$ mm^3. Most of the as-grown crystals are irregular in shape and dark-greenish in color. The single-crystal sample used for SC XRD measurement was a small piece (about 0.06 mm^3) which was cut from a bigger rectangular crystal used for the magnetization measurement. The measurements of 1204 reflections gave 358 unique reflections with $R_{int}=0.054$ and $I>2\sigma(I)$. The refinement method used is the full-matrix least squares on F^2, with the

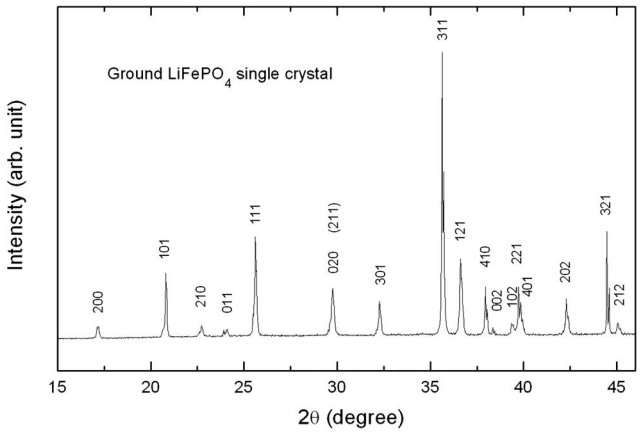

FIG. 2. The powder XRD pattern of the ground $LiFePO_4$ single crystal. The wavelength of the Cu $K\alpha$ radiation used was about 1.5406 Å.

goodness-of-fit on F^2 to be 1.123. The refinement result indicates that the crystal has orthorhombic crystal structure with space group *Pnma* (No. 62) and $Z=4$, and the lattice parameters are $a=10.3172(11)$ Å, $b=6.0096(8)$ Å, and $c=4.6775(4)$ Å. These values of lattice parameters are in good agreement with that reported in the literature[4,22–27] by other groups for their SC and polycrystalline $LiFePO_4$ samples. Figure 2 presents powder XRD pattern of a ground single crystal in the range of 2θ: $15° \leqslant 2\theta \leqslant 47°$. Note that the $K\alpha_2$ lines are not removed from the pattern. All of the lines in the pattern can be indexed with the orthorhombic structure of space group *Pnma*.

Our result of the crystal structure of $LiFePO_4$ is basically consistent with the earlier single-crystal XRD results reported by Streltsov *et al.*,[22] i.e., the cations occupy three different positions: an octahedral (Fe) site, an octahedral (Li) site, and a tetrahedral (P) site. In Table I, we list the obtained atomic coordinates for Li, Fe, P, and O. Table II summarizes the values of the Fe-O, P-O, and Li-O bond lengths for the FeO_6, PO_4, and LiO_6 polyhedra, respectively, and Table III lists all of the O-Fe-O bond angles of the FeO_6 octahedra. For a FeO_6 octahedron, Table II shows that there are four different Fe-O bond lengths ranging from 2.064 to 2.245 Å, which correlate well with those reported in the literature.[4,22,23,25,26] Table III shows that except for the two equatorial O-Fe-O angles which are far from 90° [i.e., 119.39° for the $O(3)^{i}$-Fe-$O(3)^{ii}$ and 65.99° for the $O(3)^{iv}$-Fe-$O(3)^{iii}$ angle, respectively], all of the other O-Fe-O bond angles between two neighboring Fe-O bonds are within 10° of a right angle. The different values of the Fe-O bond lengths and the substantial deviations of the two equatorial bond angles from 90° clearly indicate that the FeO_6 octahedra are highly distorted [see Fig. 1(c)]. Note that in Fig. 1(c), none of the three axes (i.e., *a*, *b*, and *c* axis) of the unit cell are along the directions of the three axes (i.e., x', y', and z' axis) of the octahedron.

TABLE I. Atomic coordinates and equivalent isotropic displacement parameter U_{eq} for $LiFePO_4$ single crystal. U_{eq} is defined as one-third of the trace of the orthogonalized U_{ij} tensor.

Atom	*x*	*y*	*z*	U_{eq} (Å^2)
Li	0	0	0	0.021(1)
Fe	0.2820(1)	0.2500	0.9751(1)	0.011(1)
P	0.0948(1)	0.2500	0.4182(2)	0.010(1)
O(1)	0.0969(2)	0.2500	0.7426(4)	0.013(1)
O(2)	0.4572(2)	0.2500	0.2056(5)	0.012(1)
O(3)	0.1655(1)	0.0465(2)	0.2849(3)	0.013(1)

TABLE II. Bond lengths (Å). Symmetry transformations used to generate equivalent atoms: (i) $-x+1/2$, $-y$, $z+1/2$; (ii) $-x+1/2$, $y+1/2$, $z+1/2$; (iii) x, y, $z+1$; (iv) x, $-y+1/2$, $z+1$; (v) $x-1/2, y$, $-z+1/2$; (vi) x, $-y+1/2$, z; (vii) x, y, $z-1$; (viii) $-x$, $-y$, $-z+1$; (iv) $-x+1/2$, $-y$, $z-1/2$; (x) $-x$, $-y$, $-z$.

Atom–atom	Distance	Atom–atom	Distance
	Fe octahedron		
Fe-$O(3)^{i}$	2.064(2)	Fe-$O(3)^{ii}$	2.064(2)
Fe-$O(2)^{iii}$	2.105(2)	Fe-O(1)	2.197(2)
Fe-$O(3)^{iii}$	2.245(2)	Fe-$O(3)^{iv}$	2.245(2)
	P tetrahedron		
P-O(1)	1.518(2)	P-$O(2)^{v}$	1.533(2)
P-O(3)	1.554(2)	P-$O(3)^{vi}$	1.554(2)
	Li octahedron		
Li-$O(1)^{vii}$	2.169(1)	Li-$O(1)^{viii}$	2.169(1)
Li-$O(2)^{v}$	2.085(2)	Li-$O(2)i^{v}$	2.085(2)
Li-O(3)	2.184(1)	Li-$O(3)^{x}$	2.184(1).

B. Anisotropy in magnetic properties

1. Experimental results: Anisotropy in magnetic susceptibility $\chi(T)$

Figure 3 shows the temperature dependent magnetic susceptibility $\chi(T)$ curves measured on a $LiFePO_4$ single-crystal sample with dimensions of $0.7\times1.6\times2.6$ mm^3 and mass of 10.4 mg. The sample was cut in a rectangular shape, with the

TABLE III. Bond angles (deg) formed between Fe-O bonds for the Fe octahedron.

Atom–atom–atom	Angle (deg)	Atom–atom-atom	Angle (deg)
$O(3)^{i}$-Fe-$O(3)^{ii}$	119.39(9)	$O(3)^{ii}$-Fe-$O(3)^{iv}$	87.06(3)
$O(3)^{iv}$-Fe-$O(3)^{iii}$	65.99(7)	$O(3)^{iii}$-Fe-$O(3)^{iii}$	87.06(3)
$O(3)^{i}$-Fe-$O(2)^{iii}$	89.72(5)	$O(3)^{ii}$-Fe-$O(2)^{iii}$	89.72(5)
$O(3)^{iv}$-Fe-$O(2)^{iii}$	97.42(6)	$O(3)^{iii}$-Fe-$O(2)^{iii}$	97.42(6)
$O(3)^{i}$-Fe-O(1)	90.87(5)	$O(3)^{ii}$-Fe-O(1)	90.87(5)
$O(3)^{iv}$-Fe-O(1)	81.61(6)	$O(3)^{iii}$-Fe-O(1)	81.61(6)
$O(3)^{i}$-Fe-$O(3)^{iv}$	152.74(7)	$O(3)^{ii}$-Fe-$O(3)^{iii}$	152.74(7)
O(1)-Fe-$O(2)^{iii}$	178.84(7)		

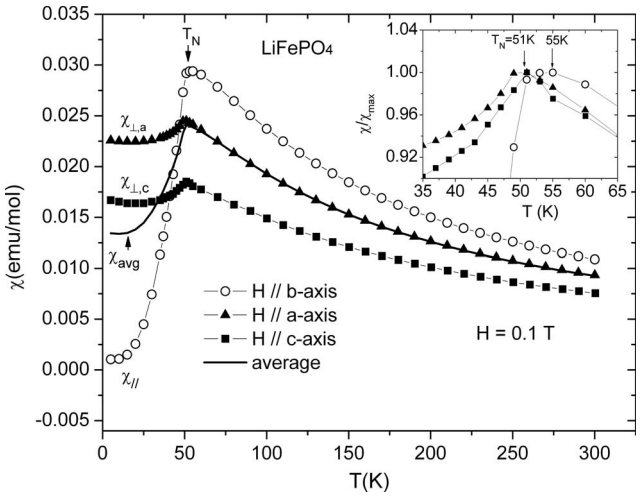

FIG. 3. Temperature dependent dc magnetic susceptibility curves measured in a field of 0.1 T and with field along the three axes of the unit cells: $\chi_{\perp,a}$ (solid triangles), $\chi_{\parallel}$ (open circles), and $\chi_{\perp,c}$ (solid squares). The solid curve is the average magnetic susceptibility χ_{avg}, defined by $\chi_{\text{avg}}=(\chi_{\parallel}+\chi_{\perp,a}+\chi_{\perp,c})/3$. The inset shows the magnified region near the peaks of the χ curves, with each curve normalized to the value at the maximum.

three axes of the unit cell along the edges of the rectangle. Hereafter, we denote the directions of the b axis (the easy axis), a axis, and c axis by symbols $\parallel$, $(\perp,a)$, and $(\perp,c)$, and the $\chi(T)$ with applied field along these three directions are denoted by $\chi_{\parallel}$, $\chi_{\perp,a}$, and $\chi_{\perp,c}$, respectively. In Fig. 3, the data points of these three $\chi(T)$ curves are shown, and the solid curve represents the χ_{avg}, defined by $\chi_{\text{avg}}=\frac{1}{3}(\chi_{\parallel}+\chi_{\perp,a}+\chi_{\perp,c})$. The $\chi(T)$ curves show that $LiFePO_4$ is antiferromagnetically (AFM) ordered. The ordering temperatures or Néel temperatures (T_N), determined by the temperature at the maximum[37] of a $\chi(T)$ curve, are about 51 K for both the $\chi_{\perp,a}$ and $\chi_{\perp,c}$ curves. For the $\chi_{\parallel}$ curve, even though its maximum is located at a slightly higher temperature, 55 K, $\chi_{\parallel}$ starts to drop much more sharply at 51 K. This can be clearly seen from the inset of Fig. 3. For this reason, we assign $T_N=51$ K for the $\chi_{\parallel}$ curve. The same value of T_N for the three directions is consistent with the observation that the peak positions (which is another way to define T_N) in the curves of the derivative of the susceptibility, $d\chi/dT$, are all located at the same temperature 47 K.

The $\chi(T)$ curves in Fig. 3 show strong magnetic anisotropy both below T_N (in the AFM ordered phase) and above T_N (in the paramagnetic phase). In the AFM ordered phase, $\chi_{\parallel}$ decreases sharply with decreasing temperature, and it almost approaches zero at 5 K. This behavior is in sharp contrast to the two $\chi_{\perp}$ curves which decrease only slightly when passing T_N and stay almost constant below 30 K. This result indicates that the easy axis for the antiferromagnetic ordering in $LiFePO_4$ is the b axis. The sharp difference in the temperature dependences between the parallel and perpendicular magnetic susceptibility curves below T_N is typical for antiferromagnetic single crystals and can be explained by the standard two-sublattice molecular field (mean field) theory of antiferromagnetism.[37,38] However, it is observed from Fig. 3 that the $\chi_{\perp,a}$ curve below T_N also exhibits a big deviation from the $\chi_{\perp,c}$ curve, indicating that a certain degree of magnetic anisotropy also exists between the two $\chi_{\perp}$ curves. Such anisotropy cannot be explained by the standard two-sublattice molecular field theory of antiferromagnetism.[37,38]

Above T_N, the three $\chi(T)$ curves do not coincide, indicating that the magnetic anisotropy in the paramagnetic phase exists not only between the parallel susceptibility and the perpendicular susceptibilities, but also between the two $\chi_{\perp}$ curves. The different slopes of the three $\chi(T)$ curves above T_N also indicate that there exists a certain anisotropy in the Lande g-factor, effective moment, and paramagnetic Curie temperature θ. These magnetic anisotropies in the paramagnetic regime (above T_N) cannot be explained by the standard, simple molecular field theory of antiferromagnetism, because such theory would predict that $\chi_{\parallel}$ and $\chi_{\perp}$ curves coincide above T_N.[37,38] Thus, the development of a theoretical model and calculation are needed to explain these anisotropies observed from the magnetic susceptibility curves of single-crystal $LiFePO_4$.

2. *Theory of the magnetic susceptibility of single-crystal* $LiFePO_4$

The anisotropy in magnetic susceptibility of $LiFePO_4$ has not been discussed theoretically. We would like to perform a theoretical calculation on the $\chi(T)$ curves with a similar approach that Homma[39] and Lines[40] developed for explaining the anisotropy in magnetic susceptibility of FeF_2. The anisotropy observed in the g-factor (see Sec. III B 3 below) for our $LiFePO_4$ single-crystal sample suggests that spin-orbit coupling should be included in the starting Hamiltonian. Very recently, Li *et al.*[34] performed a neutron scattering measurement on single-crystal $LiFePO_4$ and proposed the following Heisenberg-like Hamiltonian to explain the observed spin-wave dispersion:

$$\mathcal{H}_0 = -J_1\sum_{i,\delta}(\mathbf{S}_i\cdot\mathbf{S}_{i+\delta}) - J_2\sum_{i,\xi}\mathbf{S}_i\cdot\mathbf{S}_{i+\xi} - J_\perp\sum_{i,\eta}\mathbf{S}_i\cdot\mathbf{S}_{i+\eta} + D\sum_i (S_{iz})^2, \quad (1)$$

where J_1 is the intralayer NN superexchange (SE) interaction, J_2 is the intralayer NNN super-superexchange (SSE) interaction, $J_\perp$ is the interlayer SSE interaction, and D is the single-ion anisotropy parameter.[34] In Fig. 2(b), J_1, J_2, and $J_\perp$ are labeled. In this model, only the three J's (i.e., J_1, J_2, and $J_\perp$) corresponding to the three shortest Fe-Fe separations[41] were included. The other J's were ignored by considering that spin-spin coupling usually is weakened with increasing Fe-Fe separation. The values of these parameters determined from fitting the spin-wave dispersion data[34] were $J_1=-0.662$ meV, $J_2=-0.27$ meV, $J_\perp=0.021$ meV, and $D=-0.37$ meV. The numbers of equivalent Fe^{2+} ($S=2$) spin neighbors, z_i, corresponding to the same spin-exchange parameter J_i are $z_1=4$ for J_1, $z_2=2$ (along the c axis) for J_2, and $z_\perp=2$ for $J_\perp$, respectively.

Assuming that the x, y, and z directions are along the a axis, c axis, and b axis, respectively, we propose an exten-

sion of Eq. (1) as the Hamiltonian in the presence of an external magnetic field $\boldsymbol{H}$:

$$\mathcal{H} = \mathcal{H}_0 + \mathcal{H}_f = \sum_i \mathcal{H}_i, \tag{2}$$

where $\mathcal{H}_0$ is expressed by Eq. (1) and $\mathcal{H}_f$ is the field related part of the Hamiltonian:

$$\mathcal{H}_f = \sum_i [-\mu_B(g_{\perp,a}S_{ix}H_x + g_{\perp,c}S_{iy}H_y + g_{\parallel}S_{iz}H_z) - \mu_B^2(\Lambda_{\perp,a}H_x^2 + \Lambda_{\perp,c}H_y^2 + \Lambda_{\parallel}H_z^2)], \tag{3}$$

with g_α and Λ_α given by

$$g_\alpha = 2(1 - \lambda\Lambda_\alpha), \tag{4}$$

$$\Lambda_\alpha = \sum_n{}' \frac{|\langle 0|L_\alpha|n\rangle|^2}{E_n - E_0}, \tag{5}$$

where λ is the spin-orbit coupling constant, L_α (α=1, 2, and 3) are the orbital angular momentum component operators,[39,42] and $|n\rangle$ refer to the orbital states corresponding to energy E_n. For $LiFePO_4$, $g_\alpha > 2$ because λ is negative when a transition metal ion (d^6 for Fe^{2+}) has more than five d electrons.[36]

Parallel magnetic susceptibility. First, we derive the temperature dependence of the magnetic susceptibility for $T > T_N$, i.e., in paramagnetic state. When the external magnetic field is along the b axis (or z axis), $H=H_z$, the molecular-field Hamiltonian for the ith spin is

$$\mathcal{H}_i = -(z_1J_1 + z_2J_2 + z_\perp J_\perp)\bar{S}S_{iz} + DS_{iz}^2 - g_\parallel\mu_B S_{iz}H - \mu_B^2\Lambda_\parallel H^2. \tag{6}$$

The eigenenergies are given by

$$E_m = -m(z_1J_1 + z_2J_2 + z_\perp J_\perp)\bar{S} + m^2D - mg_\parallel\mu_B H - \mu_B^2\Lambda_\parallel H^2, \tag{7}$$

where the azimuthal quantum number m takes values of 0, ± 1, and ± 2.

The molar parallel magnetic susceptibility $\chi_\parallel$ is given by[42]

$$\chi_\parallel = N_A k_B T(\partial^2 \ln Z/\partial H^2), \tag{8}$$

where Z is the partition function:

$$Z = \sum_m \exp(-E_m/k_BT). \tag{9}$$

For $T > T_N$, if we use the experimental data (see next section) T_N=51 K, H=0.1 T, and the values of the spin-spin exchange interactions J, then both $-(z_1J_1+z_2J_2+z_\perp J_\perp)\bar{S}$ and $\mu_B H$ are much smaller than k_BT. Then, we have

$$\chi_\parallel = 2N\mu_B^2\Lambda_\parallel - (Ng_\parallel^2\mu_B^2P)/[D + (z_1J_1 + z_2J_2 + z_\perp J_\perp)P], \tag{10}$$

with

$$P = \sum_m Dm^2 \exp(-Dm^2/k_BT)/k_BT\sum_m \exp(-Dm^2/k_BT) = -1/(0.7 + k_BT/2D). \tag{11}$$

The final expression for $\chi_\parallel$ is

$$\chi_\parallel(T) = 2N\mu_B^2\Lambda_\parallel + (2Ng_\parallel^2\mu_B^2)/[k_BT + 1.4D - 2(z_1J_1 + z_2J_2 + z_\perp J_\perp)]. \tag{12}$$

This equation can be written in the form of the Curie-Weiss law:

$$\chi_\parallel(T) = \chi_{b0} + \frac{C_\parallel}{T - \theta_\parallel}, \tag{13}$$

where $\chi_{b0}=2N\mu_B^2\Lambda_\parallel$, Curie constant

$$C_\parallel = S(S+1)Ng_\parallel^2\mu_B^2/3k_B, \tag{14}$$

and

$$\theta_\parallel = -\frac{1.4D}{k_B} + \frac{S(S+1)}{3k_B}\sum_i z_iJ_i, \tag{15}$$

with S=2 for Fe^{2+}. Equation (13) is in the form of modified Curie-Weiss law, which can be used to describe other magnetic systems.[43]

Since J_1 is the NN exchange interaction and J_2 and $J_\perp$ are the NNN exchange interactions, following the similar derivations of Honma[39] and Lines,[40] we can replace z_2J_2 for FeF_2 in their derivation by $z_2J_2+z_\perp J_\perp$ for $LiFePO_4$. Then for $T > T_N$ in the antiferromagnetically ordered state, as $T \to 0$,

$$\chi_\parallel(0) = 2N\mu_B^2\Lambda_\parallel. \tag{16}$$

Perpendicular magnetic susceptibility. To derive the perpendicular magnetic susceptibility for $T > T_N$, we consider a weak magnetic field applied along the x-axis (or a-axis) direction. Since $\bar{S}_y=0$ and $\bar{S}_z=0$, the mean-field Hamiltonian can be written as

$$\mathcal{H}_i = DS_{iz}^2 - (z_1J_1 + z_2J_2 + z_\perp J_\perp)\bar{S}_xS_{ix} - g_\perp\mu_B H_xS_{ix} - \mu_B^2\Lambda_\perp H_x^2. \tag{17}$$

Following the derivation of Lines,[40] we have the following expressions for the perpendicular susceptibilities $\chi_{\perp,a}$ and $\chi_{\perp,c}$:

$$\chi_{\perp,a}(T) = 2N\mu_B^2\Lambda_{\perp,a} + (2Ng_{\perp,a}^2\mu_B^2)/[k_BT - 0.7D - 2(z_1J_1 + z_2J_2 + z_\perp J_\perp)], \tag{18}$$

$$\chi_{\perp,c}(T) = 2N\mu_B^2\Lambda_{\perp,c} + (2Ng_{\perp,c}^2\mu_B^2)/[k_BT - 0.7D - 2(z_1J_1 + z_2J_2 + z_\perp J_\perp)]. \tag{19}$$

Similarly, Eqs. (18) and (19) can be written into the Curie-Weiss Law form:

$$\chi_{\perp,a}(T) = \chi_{a0} + \frac{C_{\perp,a}}{T - \theta_{\perp,a}} \tag{20}$$

and

$$\chi_{\perp,c}(T) = \chi_{c0} + \frac{C_{\perp,c}}{T - \theta_{\perp,c}}, \tag{21}$$

where $\chi_{a0}=2N\mu_B^2\Lambda_{\perp,a}$, $\chi_{c0}=2N\mu_B^2\Lambda_{\perp,c}$, Curie constants

$$C_{\perp,a} = S(S+1)Ng_{\perp,a}^2\mu_B^2/3k_B, \tag{22}$$

$$C_{\perp,c} = S(S+1)Ng_{\perp,c}^2\mu_B^2/3k_B, \tag{23}$$

and

$$\theta_\perp = \theta_{\perp,a} = \theta_{\perp,c} = \frac{0.7D}{k_B} + \frac{S(S+1)}{3k_B}\sum_i z_i J_i. \tag{24}$$

It is interesting to note that the average value of these three θ is

$$\theta_{\text{avg}} = \frac{1}{3}\sum_{\alpha=1}^{3}\theta_\alpha = \frac{S(S+1)}{3k_B}\sum_i z_i J_i. \tag{25}$$

For comparison between the $\chi(T)$ data of single-crystal and polycrystalline samples, it is worthwhile to establish the relationship between them. Following the similar derivation of the formula for the susceptibility of the powders or polycrystalline materials, χ_{poly}, in Ref. 38, we have

$$\chi_{\text{poly}} = \tfrac{1}{3}(\chi_\parallel + \chi_{\perp,a} + \chi_{\perp,c}) = \chi_{\text{avg}}. \tag{26}$$

If one writes χ_{poly} in the form of a modified Curie-Weiss law:

$$\chi_{\text{avg}} = \chi_{\text{poly}}(T) = \chi_0 + \frac{C_{\text{avg}}}{T - \theta_{\text{poly}}}. \tag{27}$$

Then, with the use of Eqs. (13), (20), and (21), we have

$$\chi_0 = \tfrac{1}{3}(\chi_{b0} + \chi_{a0} + \chi_{c0}) = \chi_{\text{avg}}, \tag{28}$$

$$C_{\text{poly}} = \tfrac{1}{3}(C_\parallel + C_{\perp,a} + C_{\perp,c}) = C_{\text{avg}}, \tag{29}$$

and

$$\theta_{\text{poly}} = \left(1 - \frac{C_\parallel}{3C_{\text{avg}}}\right)\theta_\perp + \left(1 - \frac{C_{\perp,a}+C_{\perp,c}}{3C_{\text{avg}}}\right)\theta_\parallel. \tag{30}$$

Note that $\theta_{\text{poly}}=\theta_{\text{avg}}$ [see Eq. (25)] only when $\theta_\perp=\theta_\parallel$. Using Eqs. (14), (22), and (23), we have

$$C_{\text{avg}} = S(S+1)Ng_{\text{avg}}^2\mu_B^2/3k_B, \tag{31}$$

with

$$g_{\text{avg}}^2 = (g_\parallel^2 + g_{\perp,a}^2 + g_{\perp,c}^2)/3. \tag{32}$$

The effective magnetic moment is

$$\mu_{\text{eff,avg}} = (8C_{\text{avg}})^{1/2}. \tag{33}$$

In the next section, we will fit the experimental susceptibility curves by Eqs. (13), (20), (21), and (27) to obtain the values of Curie temperatures, Curie constants, and effective moments, and use the above theoretical results to evaluate the values of the following ten parameters: J_1, J_2, $J_\perp$, D, $g_{\perp,a}$, $g_{\perp,c}$, $g_\parallel$, $\Lambda_{\perp,a}$, $\Lambda_{\perp,c}$, and $\Lambda_\parallel$.

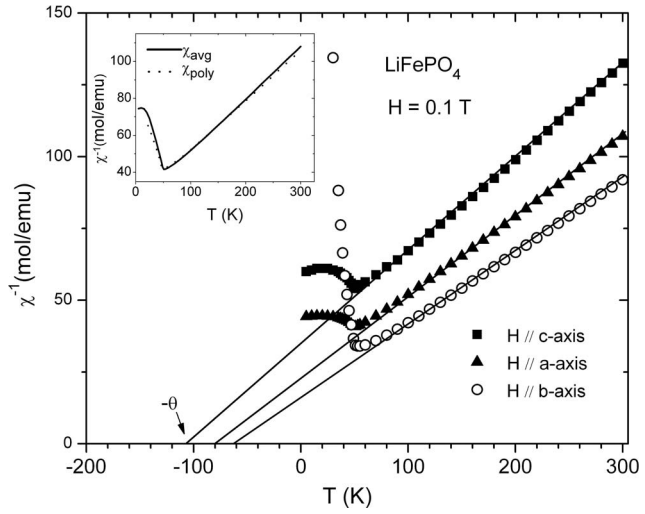

FIG. 4. The plots of the inverse susceptibilities $\chi_{\perp,a}^{-1}$ (solid triangles), $\chi_\parallel^{-1}$ (open circles), and $\chi_{\perp,c}^{-1}$ (solid squares) against temperature. The straight, solid lines through the χ^{-1} data points are the linear fits of the data to $\chi^{-1}=(T-\theta_p)/C$ in 70 K$\leqslant T\leqslant$300 K. Inset: $\chi_{\text{avg}}^{-1}(T)$ curve in comparison with the $\chi_{\text{avg}}^{-1}(T)$ curve taken from Ref. 46.

3. *Fitting results for the $\chi(T)$ curves and discussions*

The anisotropy in the g-factor and θ can be studied by fitting the $\chi(T)$ curves above T_N by Eqs. (13), (20), and (21), or by fitting the inverse susceptibility curves to $(\chi_\alpha-\chi_{\alpha 0})^{-1}=(T-\theta_\alpha)/C_\alpha$, with $\alpha=1,2,3$ corresponding to $\parallel$, $(\perp,a)$, and $(\perp,c)$, in the temperature range of 70 K$\leqslant T\leqslant$300 K. The fitting lines are shown in Fig. 4 by the solid lines. The fitting is done self-consistently, i.e., the values of g_α and Λ_α obtained from the fitting should be consistent with that given by Eqs. (4) and (16). The values of the effective moment $[\mu_{\text{eff}}=(8C_\alpha)^{1/2}]$ are determined from the fitting values of the Curie constant C_α. To calculate the g-factors, $S=2$ for Hund's rule ground state ($^5D_4$) of free Fe^{2+} (d^6) ions is used. Since the spin-wave theory of antiferromagnetism[44] predicts a T^2 dependence of $\chi_\parallel(T)$ at low temperature, the value of $\chi_\parallel(0)$ is obtained by fitting the $\chi_\parallel(T)$ data to $\chi_\parallel(T)=a+bT^2$ in the range of $5\leqslant T\leqslant 20$ K and extrapolated to $T=0$. We have the following fitting results:

(i) for $\chi_\parallel(T)=\chi_{b0}+C_\parallel/(T-\theta_\parallel)$, $\chi_{b0}=\chi_\parallel(0)=7.2\times10^{-4}$ emu/mol, $C_\parallel=3.685$ emu K/mol, and $\theta_\parallel=-59.7\pm1.7$ K, which yield $g_\parallel=2.22$, $\Lambda_\parallel=1.38\times10^{-3}$ cm, and $\mu_{\text{eff},\parallel}=5.43\pm0.02\ \mu_B$;

(ii) for $\chi_{\perp,a}(T)=\chi_{a0}+C_{\perp,a}/(T-\theta_{\perp,a})$, $\chi_{a0}=4.41\times10^{-4}$ emu/mol, $C_{\perp,a}=3.412$ emu K/mol, and $\theta_{\perp,a}=-80.9\pm1.3$ K, which yield $g_{\perp,a}=2.13$, $\Lambda_{\perp,a}=8.46\times10^{-4}$ cm, and $\mu_{\text{eff},\perp,a}=5.22\pm0.02\mu_B$; and

(iii) for $\chi_{\perp,c}(T)=\chi_{c0}+C_{\perp,c}/(T-\theta_{\perp,c})$, $\chi_{c0}=6.30\times10^{-5}$ emu/mol, $C_{\perp,c}=3.058$ emu K/mol, and $\theta_{\perp,c}=-105.7\pm1.5$ K, which yield $g_{\perp,c}=2.02$, $\Lambda_{\perp,c}=1.21\times10^{-4}$ cm, and $\mu_{\text{eff},\perp,c}=4.95\pm0.02\mu_B$.

The value of λ obtained from the fitting is -78.30 cm^{-1}. The values of the θ_{avg}, defined by Eq. (25), and $\theta_\perp$, defined by $\theta_\perp=(\theta_{\perp,a}+\theta_{\perp,c})/2$, are thus $\theta_{\text{avg}}=-82.1$ K and $\theta_\perp=(\theta_{\perp,a}+\theta_{\perp,c})/2=-93.3$ K, respectively. The average values

TABLE IV. The values of T_N and the result of fitting magnetic susceptibility curves to the modified Curie-Weiss law for single-crystal $LiFePO_4$.

Axis	T_N (K)	C (emu K/mol)	θ (K)	g	Λ (cm)	μ_{eff} (μ_B)
b ($\parallel$)	51	3.685	-59.7 ± 1.7	2.22	0.00138	5.43 ± 0.02
a ($\perp, a$)	51	3.412	-80.9 ± 1.3	2.13	0.00085	5.22 ± 0.02
c ($\perp, c$)	51	3.058	-105.7 ± 1.5	2.02	0.00012	4.95 ± 0.02
Average	51	3.385	-82.1 ± 1.5	2.12	0.00076	5.20 ± 0.02

of C, g, and μ_{eff} calculated using Eqs. (29), (32), and (33) and the above fitting values are $C_{\text{avg}}=3.385$ emu K/mol, $g_{\text{avg}}=2.12$, and $\mu_{\text{eff,avg}}=5.20\mu_B$. The fitting results are summarized in Table IV. These results indicate a strong anisotropy for the g-factor and the paramagnetic Curie temperature θ. The μ_{eff} values obtained from the fitting are within a 7% deviation from the values measured previously by Creer and Troup[45] and are 13%–20% smaller than those reported recently by Chen *et al.*[30] Compared with their data, our value for $\theta_{\parallel}$ (−59.7 K) is very close to that (=−68 ± 10 K) measured by Creer and Troup,[45] but substantially higher (i.e., less negative) than the value (−105.7 K) measured by Chen *et al.*;[30] our values for both $\theta_{\perp,a}$(=−80.9 K) and $\theta_{\perp,c}$ (=−105.7 K) are substantially higher (~30%–40% higher) than the values reported by these two groups.

We would like to compare the $\chi^{-1}(T)$ data reported by Santoro and Newman[46] for their polycrystalline $LiFePO_4$ samples with our single-crystal data. For this purpose, we plotted the inverse of the average magnetic susceptibility $\chi^{-1}_{\text{avg}}(T)$ in the inset of Fig. 4 in comparison with the $\chi^{-1}_{\text{poly}}(T)$ curve (dotted curve in Fig. 4) reported by Santoro and Newman[46] Here, the $\chi^{-1}_{\text{avg}}(T)$ is calculated from the $\chi_{\text{avg}}(T)$ curve in Fig. 3. The inset of Fig. 4 shows that our $\chi^{-1}_{\text{avg}}(T)$ curve for single crystal matches well with the $\chi^{-1}_{\text{poly}}(T)$ curve, demonstrating the validity of the derived relationship $\chi_{\text{avg}}(T)=\chi_{\text{poly}}(T)$.

The average value of T_N, obtained from the maximum of the χ_{avg} curve shown in Fig. 3, is $T_{N,\text{avg}}=51 \pm 2$ K. This $T_{N,\text{avg}}$ value is very close to the values (≈50 ± 2 K) reported in the literature[46–48] for polycrystalline samples. Fitting the $\chi^{-1}_{\text{avg}}(T)$ curve in the inset of Fig. 4 to the modified Curie-Weiss law [Eq. (27)] $\chi_{\text{avg}}(T)=\chi_0+C_{\text{avg}}/(T-\theta_{\text{poly}})$, with $\chi_0=3.984\times10^{-4}$ emu/mol given by Eq. (28), we have the following values: $C_{\text{avg}}=3.371$ emu K/mol, $\theta_{\text{poly}}=-78.0 \pm 1.5$ K, $g=2.12$, and $\mu_{\text{eff}}=5.19 \pm 0.02$ μ_B. The fitting values for g and μ_{eff} are the same as those estimated above (listed in Table IV). The fitting value of $\theta_{\text{poly}}=-78.6 \pm 1.5$ K is almost the same as the value (−81.1 K) estimated from Eq. (30) with the use of the fitting results described above. The fitting value ($5.19\mu_B$) of μ_{eff} is slightly greater than the "spin-only" [i.e., with orbital angular momentum L fully quenched by crystal field (CF)] moment $4.90\mu_B$ for the high-spin state ($S=2$) of Fe^{2+} (d^6) ion[37] and substantially smaller than the free ion value of $6.71\mu_B$ calculated from the total angular momentum $J=L+S$, indicating that the Fe ions in the crystal are divalent and their orbital moments are substantially quenched by CF. The value of μ_{eff} observed here is in good agreement with those observed in other compounds containing Fe^{2+} ions, such as FeO ($5.33\mu_B$), FeF_2 ($5.59\mu_B$), $FeCl_2$ ($5.38\mu_B$), FeS ($5.24\mu_B$), $KFeCl_3$ ($5.50\mu_B$), and $BaLa_2FeS_5$ ($5.41\mu_B$).[49–53] The values of the $-\theta_{\text{poly}}$ (≈78.0 K) and μ_{eff} ($5.19\mu_B$) estimated here for our single-crystal $LiFePO_4$ samples are quite close to the values ($-\theta=88$ K and $\mu_{\text{eff}}=5.45\mu_B$) obtained by Santoro[46] for his polycrystalline samples, but considerably less than the values ($-\theta=115$ K and $\mu_{\text{eff}}=5.85\mu_B$) reported recently by Arcon *et al.*[48]

Now, let us examine the values of the spin-exchange constants J_1, J_2, and $J_\perp$, and the anisotropy parameter D. If we use the values of these constants and/or parameter obtained from the neutron scattering measurement,[34] i.e., $J_1=-0.662$ meV, $J_2=-0.27$ meV, $J_\perp=0.021$ meV, and $D=-0.37$ meV, then Eqs. (15), (24), and (25) give $\theta_{\parallel}=-67.0$ K, $\theta_\perp=(\theta_{\perp,a}+\theta_{\perp,c})/2=-76.0$ K, and $\theta_{\text{avg}}=-73.0$ K, respectively. Even though the value of $\theta_\perp$ is 17.3 K smaller in magnitude (or less negative) than the value of −93.3 K obtained from fitting the $\chi_\perp$ data to the modified Curie-Weiss law, the values of θ_{avg} and $\theta_{\parallel}$ calculated using these values of J's and D are in good agreement (i.e., within 11% discrepancy) with the values ($\theta_{\text{avg}}=-82.1$ K and $\theta_{\parallel}=-59.7$ K) obtained from the fitting.

Figure 5 shows the field dependent molar magnetization $M(H)$ curves for the single-crystal $LiFePO_4$ sample, measured at different temperatures (i.e., 5, 35, 45, and 50 K) below T_N and with the magnetic field $\boldsymbol{H}$ along the directions of the a, b, and c axes of the unit cell. Figures 5(a)–5(c) display the $M(H)$ data measured with field varying from 0 to 5 T. The linear dependence of M on H for all of the plots indicates that there is no spin flip or spin flop[54] in the antiferromagnetic phase in fields up to 5 T. The slopes of the $M(H)$ straight lines in the 0–5 T range match well with the corresponding magnetic susceptibility data (measured at 0.1 T) shown in Fig. 3. Figure 5(d) displays the $M(H)$ hysteresis loops measured at 5 and 35 K and with the field varying via $0\rightarrow5$ T$\rightarrow-5$ T$\rightarrow5$ T. All of the curves are reversible. This absence of magnetic hysteresis in this field range is consistent with the observed linearity between M and H.

C. Polarized x-ray absorption spectroscopy results

The single-crystal sample used for the XAS measurement is the same sample used for magnetic susceptibility measurements. In Fig. 6, we show the polarized Fe K-edge spectra for this $LiFePO_4$ single-crystal sample, with x-ray polarization vector $\boldsymbol{E}$ parallel to the three axes of the unit cell. In the

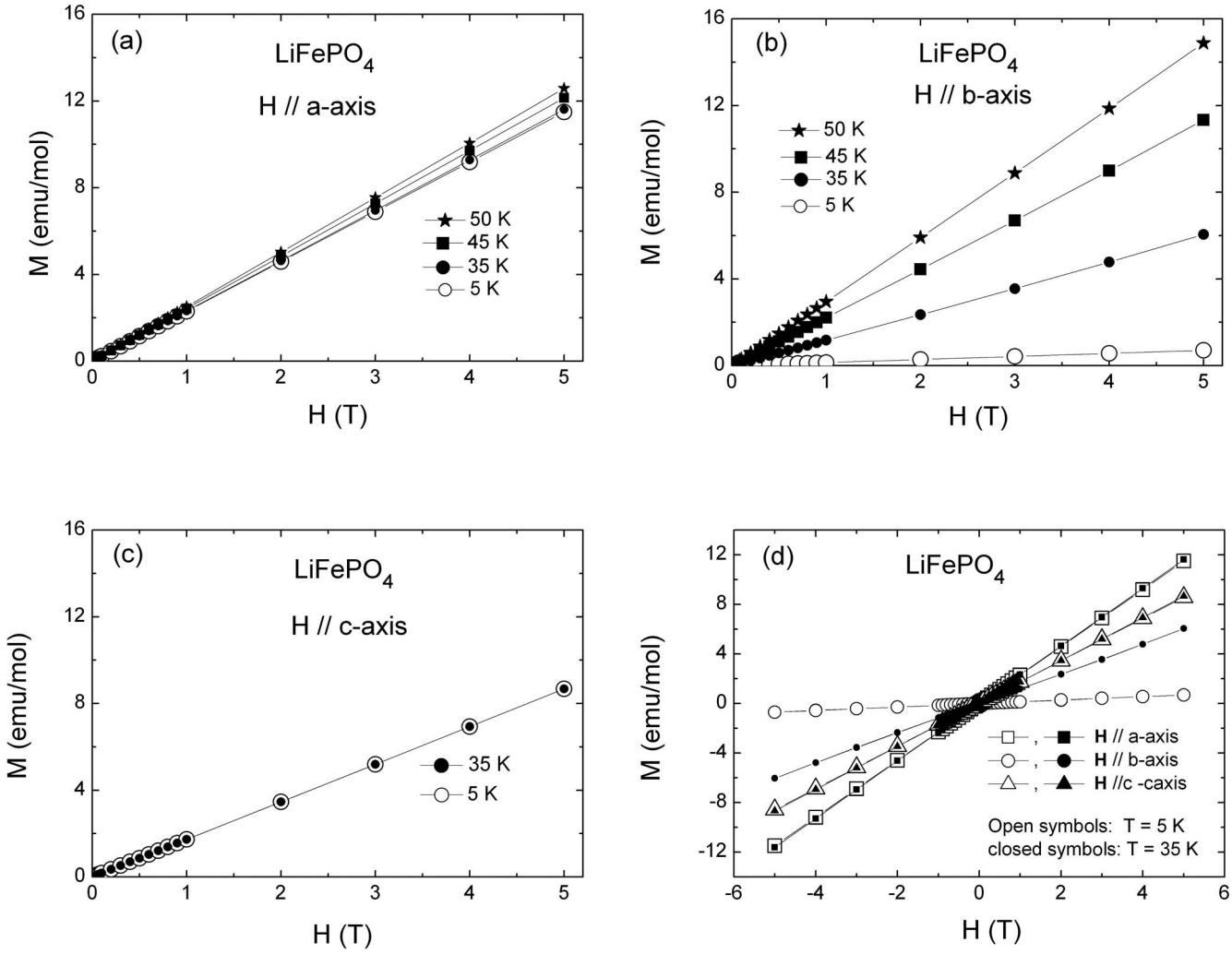

FIG. 5. [(a)–(c)] Field (H) dependent magnetization (M) for the single-crystal $LiFePO_4$ sample measured at different temperatures and with field varying from 0 to 5 T. (d) The $M(H)$ curves measured with field varying from $0 \rightarrow 5$ T $\rightarrow -5$ T $\rightarrow 5$ T, at two temperatures: 5 and 35 K.

measurement, the orientations of the axes of the sample were arranged as follows: (a) for $\boldsymbol{E} \| b$ axis, $\boldsymbol{k} \| a$ axis; (b) for $\boldsymbol{E} \| a$ axis, $\boldsymbol{k} \| c$ axis; and (c) for $\boldsymbol{E} \| c$ axis, $\boldsymbol{k} \| a$ axis. The three polarized spectra in Fig. 6 show different edge energies and display different shapes, indicating a certain degree of anisotropy in the electronic structure near the Fermi level. Basically, the polarized spectra shown in Fig. 6 consist of two main regions: the low-energy region where the preedge "*a* feature" is located and the main edge region where the features labeled by $A_\pi - C_\sigma$ are located. The symmetries and energies of the electronic final states and the selection rules of quantum transition strongly affect the positions and intensities of the absorption features of polarized x ray near the Fe *K* edge. Previously, Westre *et al.*[55] studied some octahedral oxygen-coordinated Fe (II) compounds, and Hass *et al.*[56] and other groups[4,25,57–62] recently studied polycrystalline $LiFePO_4$ samples by unpolarized Fe *K*-, Fe *L*-, and O *K*-edge XAS measurements. Similar to the feature assignments for the Fe *K*-edge spectra in some of these studies, we can assign the preedge *a* feature as due to the dipole forbidden (but quadrupole allowed, see below) Fe$1s \rightarrow 3d$ transition and the features on the main edge as $1s \rightarrow 4p$ transitions.

The relative positions and intensities of the features $A_\pi - C_\sigma$ in the main edge region of the spectra (see Fig. 6) are similar to what were previously observed from the polarized Cu and Ni *K*-edge spectra of some cuprate and nickelate compounds, such as $Nd_{2-x}Ce_xCuO_4$ $(0 \leqslant x \leqslant 0.18)$, $IBi_2Sr_2CuO_2$ and $La_{2-x}Sr_xCuO_4$ $(0 \leqslant x \leqslant 1)$, and $La_{2-x}Sr_xNiO_4$ $(0 \leqslant x \leqslant 1)$ series,[63–66] which have either octahedral or square planar coordination of oxygen ligands about the central transition metal ions. Thus, we propose here a feature assignment for the polarized Fe *K*-edge spectra of $LiFePO_4$, similar to the feature assignments we previously made on polarized Cu and Ni *K*-edge spectra.[63–66] The features A_π and B_π in the $\boldsymbol{E} \| c$ spectrum are assigned to the transition from $1s$ to out-of-plane $4p_\pi$ state transitions, whereas the B_σ and C_σ in the $\boldsymbol{E} \| b$ spectrum are due to the transitions of electrons from $1s$ to in-plane $4p_\sigma$ states. The lower-energy features A_π and B_σ involve "shake down" final states in which the core hole is better screened (relative to the B_π and C_σ related processes) by the transfer of a ligand electron to the well localized $3d$ shell.[63] These final states

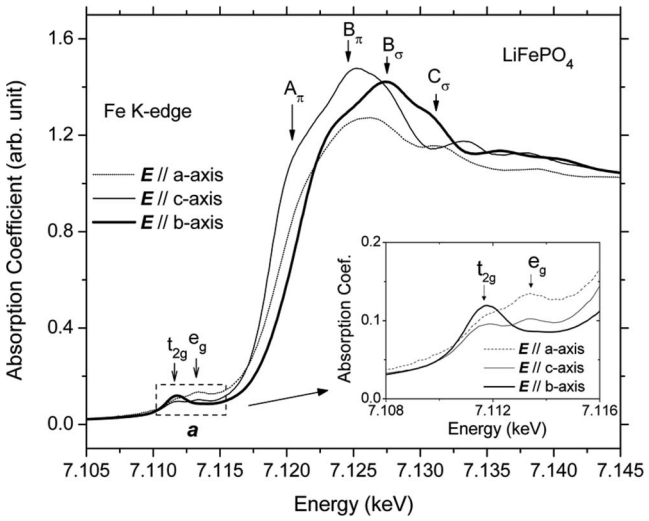

FIG. 6. Polarized x-ray absorption spectra at the Fe K edge for the single-crystal $LiFePO_4$, with the polarization vector $\boldsymbol{E}$ of the x-ray radiation parallel to the a axis (dashed curve), c axis (thinner solid curve), and b axis (thicker solid curve). The feature assignment is discussed in text.

can be denoted by $3d^7\underline{L}$, where $\underline{L}$ denotes a ligand shell hole. The higher-energy features B_π and C_σ can be associated with the unscreened $3d^6$ final states.

It appears that the $\boldsymbol{E}\|a$ spectrum in Fig. 6 contains all four $1s\rightarrow 4p$ transition features A_π–C_σ. Qualitatively, this can be understood by the deviation of the a axis from the z' axes [see Fig. 1(c)] of the FeO_6 octahedra. Due to this deviation, the in-plane and out-of-plane components of the polarization vector $\boldsymbol{E}$ in the $\boldsymbol{E}\|a$ case can excite transitions of electrons from $1s$ to the $4p_\pi$ and $4p_\sigma$ states, respectively. Similarly, the smaller intensity of the B_σ feature evidenced in the $\boldsymbol{E}\|c$ spectrum can also be explained by the in-plane component of the $\boldsymbol{E}$ due to the deviation of the c axis from the equatorial planes of the FeO_6 octahedra. The values of the edge energy E_{edge}, which is defined as the energy at which the absorption coefficient=0.5, are 7118.2, 7118.8, and 7119.6 eV, respectively, for the $\boldsymbol{E}\|c$, $\boldsymbol{E}\|a$, and $\boldsymbol{E}\|b$ spectra. The observed difference in edge energy for these spectra can be attributed to the variation of the intensity of the A_π feature. For the $\boldsymbol{E}\|b$ spectrum, the edge energy is the highest due to the absence of the A_π feature. These edge energies are very close to those for divalent iron compounds such as the reference compound FeO (which has E_{edge}=7119.0 eV) used in this study, indicating that the Fe ions in single-crystal $LiFePO_4$ are divalent. This result is in agreement with the effective magnetic moment of Fe^{2+} ion estimated from the magnetic susceptibility curves.

A detailed examination reveals that the preedge feature A is actually a feature with double bumps, which are labeled by t_{2g} and e_g, and is enlarged in the inset of Fig. 6. The lower-energy t_{2g} feature located at about 7111.7 eV is attributed to the Fe $1s\rightarrow 3d_{t_{2g}}$ transition, and the higher-energy e_g feature located at 7113.5 eV is due to the $1s\rightarrow 3d_{e_g}$ transition. To the first order approximation for which the distortion of the FeO_6 octahedron can be neglected, the octahedral ligand field around the Fe due to the six O ligands splits the fivefold degenerate energy of the Fe $3d$ states into two subsets: the lower, threefold t_{2g} levels and the higher, twofold e_g levels.[55,56,67] If the three axes of the FeO_6 octahedron are denoted by x', y', and z' axis, as shown in Fig. 1(c), then the two e_g states consist of the $d_{x'^2-y'^2}$ and $d_{z'^2}$ orbitals, and the three t_{2g} states consist of the $d_{x'y'}$, $d_{y'z'}$, and $d_{x'z'}$ orbitals.[67,68] In Hund's rule ground state of the Fe^{2+} ($3d^6$) ions, each of these five orbitals is filled with a spin-up electron, and a t_{2g} orbital is filled with a spin-down electron. Such an electronic configuration for the $3d^6$ is consistent with the theoretical results calculated by Shi *et al.*[47] on the density of states of the Fe $3d$ band, which predicted that the Fermi level is above the entire up-spin $3d$ subband and part of the down-spin $3d$ t_{2g} band. As discussed before, such a high-spin Hund's rule ground state of Fe^{2+} ion is also consistent with the measured effective magnetic moment for the $LiFePO_4$ single-crystal sample. Since both the t_{2g} and e_g orbitals are partially occupied, the $1s$ electrons of the Fe^{2+} ions can be excited to these two sets of $3d$ orbitals by absorption of x-ray photons. A detailed curve-fitting analysis on such double-bump preedge features for some octahedral oxygen-coordinated Fe (II) compounds by Westre *et al.*[55] indicates that such double bumps in the preedge feature are actually a superposition of three spectral peaks (corresponding to three final many-electron excited states) due to the transition of the Fe $1s$ electrons from the $1s$ orbital to the $3d$ t_{2g} and e_g orbitals.

The inset of Fig. 6 clearly shows that for both the $\boldsymbol{E}\|a$ axis and $\boldsymbol{E}\|c$ axis spectra, the intensity of the e_g features are higher than that of the t_{2g} feature. However, for the $\boldsymbol{E}\|b$ axis spectrum, the intensity of the e_g feature is much lower than that of the t_{2g} feature. Such anisotropy in the intensities of the features caused by different polarizations can be explained by the analysis of the quadrupole-term[69,70] contribution to the absorption coefficient μ. Within one-electron theory and following a similar procedure adopted by Bocharov *et al.*,[71] the electric quadrupole term of absorption coefficient μ can be derived to be

$$\mu_q = \mu_{d_{x'y'}} + \mu_{d_{x'z'}} + \mu_{d_{y'z'}} + \mu_{d_{x'^2-y'^2}} + \mu_{d_{z'^2}}, \tag{34}$$

with the following partial absorption coefficients:

$$\mu_{d_{x'y'}} = \rho_{d_{x'y'}}(E_{x'}k_{y'} + E_{y'}k_{x'})^2$$

$$\mu_{d_{x'z'}} = \rho_{d_{x'z'}}(E_{x'}k_{z'} + E_{z'}k_{x'})^2,$$

$$\mu_{d_{y'z'}} = \rho_{d_{y'z'}}(E_{y'}k_{z'} + E_{z'}k_{y'})^2,$$

$$\mu_{d_{x'^2-y'^2}} = \rho_{d_{x'^2-y'^2}}(E_{x'}k_{x'} - E_{y'}k_{y'})^2$$

$$\mu_{d_{z'^2}} = 3\rho_{d_{x'^2}}E_{z'}^2k_{z'}^2. \tag{35}$$

It is seen that the expressions for the first three partial absorption coefficients are the same as previously reported by

TABLE V. The partial absorption coefficients (in units of $\rho E^2 k^2$) for the absorption process corresponding to final $3d$ states of different orbital symmetries, evaluated from Eq. (35) for undistorted FeO_6 octahedra.

Direction of $\boldsymbol{E}$	Direction of $\boldsymbol{k}$	$\mu_{d_{x'y'}}$	$\mu_{d_{x'z'}}$	$\mu_{d_{y'z'}}$	$\mu_{d_{x'^2-y'^2}}$	$\mu_{d_{z'^2}}$	$I_{e_g}/I_{t_{2g}}$
$\boldsymbol{E} \parallel b$ axis	$\boldsymbol{k} \parallel a$ axis	0	0.365	0.365	0.254	0	0.348
$\boldsymbol{E} \parallel a$ axis	$\boldsymbol{k} \parallel c$ axis	0.189	0.121	0.121	0	0.573	1.329
$\boldsymbol{E} \parallel c$ axis	$k \parallel a$ axis	0.189	0.121	0.121	0	0.573	1.329

Bocharov *et al.*,[71] but the expressions for $\mu_{d_{x'^2-y'^2}}$ and $\mu_{d_{z'^2}}$ are different from theirs.

To estimate the values of these partial absorption coefficients for different sample orientations with respect to the directions of $\boldsymbol{E}$ and $\boldsymbol{k}$, it is necessary to specify the directions of the a, b, and c axes of the unit cell in the local $x'y'z'$ coordinate system of the FeO_6 octahedra. From Fig. 1(c), we see that the b axis is lying on the $x'y'$ plane and along the direction of an in-plane $O(3)^{i}$-$O(3)^{ii}$ bond, which is the common edge of the FeO_6 octahedron and one of the four neighboring PO_4 tetrahedra. In the discussion below, to the first order approximation, we treat the FeO_6 octahedra as undistorted, and we believe that the conclusions derived should be close to the results for a distorted octahedral. For an undistorted FeO_6 octahedron, b axis is perpendicular to the z' axis and is 45° from either the x' or the y' axis. Actually, there are two groups of FeO_6 octahedra: the first group (group 1) of octahedra is similar to that sketched in Fig. 1(c), which has its z' axis tilted about 30.2° (i.e., $\theta_{az'}$ below) away to the right of the ab planes (which are parallel to the plane formed by [001] and [010] axes); the second group (group 2) of octahedra has its z' axis tilted the same angle away from the ab planes but to the left side. From the values of the atomic coordinates of O(1) and $O(2)^{iii}$ listed in Table I, one can estimate that the z' axis [along the O(1)-$O(2)^{iii}$ line in Fig. 1(c)] makes angles of $\theta_{az'} \approx 30.2°$ and $\theta_{cz'} \approx 59.8°$ to the a axis and c axis, respectively. Thus, in the local $x'y'z'$ coordinate system, the unit polarization vectors along the positive directions of the a, b, and c axes can be expressed as $\boldsymbol{\varepsilon}_a = (\pm \sin\theta_{az'}/\sqrt{2}, \pm \sin\theta_{az'}/\sqrt{2}, \cos\theta_{az'})$, $\boldsymbol{\varepsilon}_b = (1/\sqrt{2}, -1/\sqrt{2}, 0)$, and $\boldsymbol{\varepsilon}_c = (-\sin\theta_{cz'}/\sqrt{2}, -\sin\theta_{cz'}/\sqrt{2}, \pm\cos\theta_{cz'})$, respectively, where the signs "+" and "−" are designated for the second and first group of FeO_6 octahedra, respectively.

Thus, for $\boldsymbol{E} \parallel b$ axis and $\boldsymbol{k} \parallel a$ axis, $\boldsymbol{E} = (E_{x'}, E_{y'}, E_{z'}) = (1/\sqrt{2}, -1/\sqrt{2}, 0)E$ and $\boldsymbol{k} = (k_{x'}, k_{y'}, k_{z'}) = (\pm 0.356, \pm 0.356, 0.864)k$. The partial absorption coefficients are calculated from Eq. (35) and the values are listed in Table V. Here, we assume that the characteristic resonance (Lorentzian form) factors ρ_{fi} ($\rho_{d_{x'y'}}$ etc.) in Eq. (35) are the same, i.e., $\rho_{fi} = \rho$. The intensity ratio of the e_g to t_{2g} feature in the Fe K edge, defined as $I_{e_g}/I_{t_{2g}} \propto (\mu_{d_{x'^2-y'^2}} + \mu_{d_{z'^2}})/(\mu_{d_{x'y'}} + \mu_{d_{x'z'}} + \mu_{d_{y'z'}})$, is estimated to be 0.348. This is in good agreement with what was observed in the b-polarization spectrum (see inset of Fig. 6), where the intensity of the e_g feature is much smaller than that of the t_{2g} feature. In the cases of $\boldsymbol{E} \parallel a$ axis and $\boldsymbol{E} \parallel c$ axis, the partial absorption coefficients and $I_{e_g}/I_{t_{2g}}$ are also calculated and the values are shown in Table V. Our calculation shows that for both the a- and c-polarization spectra, $I_{e_g}/I_{t_{2g}} = 1.329$. This result indicates that for these two polarizations, the intensity of the e_g feature is stronger than that of the t_{2g} feature, which is also in good agreement with the observation in the inset of Fig. 6. Thus, the anisotropy of the intensities of the features of $1s \rightarrow 3d$ quadrupole transitions due to different polarizations is explained adequately with the one-electron approximation.

IV. CONCLUSIONS

Large-size high quality $LiFePO_4$ single crystals have been grown by a flux growth technique with LiCl as flux. The as-grown single crystals have volumes up to about 300 mm^3 (~1.0 g). SC XRD measurement shows that the crystals are orthorhombic with space group *Pnma* ($Z=4$). The lattice parameters obtained from the refinement are $a = 10.3172(11)$ Å, $b = 6.0096(8)$ Å, and $c = 4.6775(4)$ Å. We also obtained the values of Fe-O bond lengths and O-Fe-O bond angles for the FeO_6 octahedron. Our SC XRD results on the $LiFePO_4$ single crystals are basically consistent with those reported previously by Streltsov *et al.*[22] The powder XRD result on the ground SC $LiFePO_4$ confirms that the single crystals are a pure phase.

The results of anisotropy in magnetic properties of single-crystal $LiFePO_4$ are reported. A mean-field theory of antiferromagnetism is developed to explain the observed strong anisotropies in g-factor, paramagnetic Curie temperature, and effective moment for $LiFePO_4$ single crystals. It is found that the values of the θ_{avg} and $\theta_{\perp}$ calculated by this theory with the use of the values of spin-spin exchange interactions (J_1, J_2, and $J_{\perp}$) and single-ion anisotropy (D) (which were obtained from previous neutron scattering measurement) match well with the values obtained from our fitting of the χ_{avg} to the modified Curie-Weiss law.

We performed the polarized XAS measurement at the Fe K edge on single-crystal $LiFePO_4$. Based on the anisotropy observed in the polarized spectra, a different feature assignment is proposed to give a qualitative explanation for the $1s \rightarrow 4p_{\pi}$ and $1s \rightarrow 4p_{\sigma}$ transition features. Such an identification of the out-of-plane $4p_{\pi}$ and in-plane $4p_{\sigma}$ electronic states in Fe K edge could provide a guide for future K-edge XAS study of other Fe compounds, particularly those with octahedral or square planar oxygen coordination. Finally, anisotropy in the intensities of the $1s \rightarrow 3d$ transition features is observed for spectra with different $\boldsymbol{E}$ polarizations, and such anisotropy is explained adequately by a one-electron-theory calculation on the electric quadrupole term of the absorption coefficient.

ACKNOWLEDGMENTS

The work at Sam Houston State University (SHSU) was supported by the National Science Foundation under Grant No. CHE-0718482, a grant from the SHSU EGR program, and a grant from Research Corporation. The work at the University of Texas at Austin is supported by the Welch Foundation under Grant No. F-1191 and by the National Science Foundation under Grant No. DMR-0605828. The work at Ames Laboratory is supported by the Department of Energy, Office of Basic Energy Sciences under Contract No. W-7405-Eng-82.

*Corresponding author: phy_gnl@shsu.edu

[1] A. K. Padhi, K. S. Nanjundaswamy, and J. B. Goodenough, J. Electrochem. Soc. **144**, 1188 (1997).
[2] H. Huang, Y. Lee, and J. B. Goodenough, J. Electrochem. Soc. **145**, 3220 (1999).
[3] S.-Y. Chung, J. Bloking, and Y.-M. Chiang, Nat. Mater. **1**, 123 (2002).
[4] G. X. Wang, S. Bewlay, S. A. Needham, H. K. Liu, R. S. Liu, V. A. Drozd, J.-F. Lee, and J. M. Chen, J. Electrochem. Soc. **153**, A25 (2006).
[5] K. Striebel, J. Shim, V. Srinivasan, and J. Newman, J. Electrochem. Soc. **152**, A664 (2005).
[6] X. Z. Liao, Z. F. Ma, L. Wang, X. M. Zhang, Y. Jiang, and Y. S. He, Electrochem. Solid-State Lett. **7**, A522 (2004).
[7] J.-M. Tarascon and M. Armand, Nature (London) **414**, 359 (2001).
[8] Yong-Nian Xu, Sung-Yoon Chung, Jason T. Blocking, Yet-Ming Chiang, and W. Y. Ching, Electrochem. Solid-State Lett. **7**, A131 (2004).
[9] Ou-Yang Chuying, Siqi Shi, Z. Wang, X. Huang, and L. Chen, Phys. Rev. B **69**, 104303 (2004).
[10] C. Y. Ouyang, S. Q. Shi, Z. X. Wang, H. Li, X. J. Huang, and L. Q. Chen, J. Phys.: Condens. Matter **16**, 2265 (2004).
[11] P. Subramanya Herle, B. Ellis, N. Coombs, and L. F. Nazar, Nat. Mater. **3**, 147 (2004).
[12] S. Shi, L. Liu, C. Ouyang, D. S. Wang, Z. Wang, L. Chen, and X. Huang, Phys. Rev. B **68**, 195108 (2003).
[13] J. F. Ni, H. H. Zhou, J. T. Chen, and X. X. Zhang, Mater. Lett. **59**, 2361 (2005).
[14] J. Molenda, Mater. Sci. (Poland) **24**, 61 (2006).
[15] H. Huang, S.-C. Yin, and L. F. Nazar, Electrochem. Solid-State Lett. **4**, A170 (2001).
[16] S. Franger, F. L. Cras, C. Bourbon, and H. Rouault, J. Power Sources **119-121**, 252 (2003).
[17] J. Yang and J. J. Xu, Electrochem. Solid-State Lett. **7**, A515 (2004).
[18] C. H. Mi, X. B. Zhao, G. S. Cao, and J. P. Tu, J. Electrochem. Soc. **152**, A483 (2005).
[19] P. Prosini, M. Carewska, S. Scaccia, P. Wisniewski, S. Passerini, and M. Pasquali, J. Electrochem. Soc. **149**, A886 (2002).
[20] F. Croce, A. D'Epifanio, J. Hassoun, A. Deptula, T. Olczac, and B. Scrosati, Electrochem. Solid-State Lett. **5**, A47 (2002).
[21] C. R. Sides, F. Croce, V. Y. Young, C. R. Martin, and B. Scrosati, Electrochem. Solid-State Lett. **8**, A484 (2005).
[22] V. A. Streltsov, E. L. Belokoneva, V. G. Tsirelson, and N. K. Hansen, Acta Crystallogr., Sect. B: Struct. Sci. **B49**, 147 (1993).
[23] P. Tang and N. A. W. Holzwarth, Phys. Rev. B **68**, 165107 (2003).
[24] A. S. Andersson, B. Kelska, L. Häggström, and J. O. Thomas, Solid State Ionics **130**, 41 (2000).
[25] A. A. M. Prince, S. Mylswamy, T. S. Chan, R. S. Liu, B. Hannoyer, M. Jean, C. H. Shen, S. M. Huang, J. F. Lee, and G. X. Wang, Solid State Commun. **132**, 455 (2004).
[26] G. Rousse, J. Rodriguez-Carvajal, S. Patoux, and C. Masquelier, Chem. Mater. **15**, 4082 (2003).
[27] J. M. Osorio-Guillén, B. Holm, R. Ahuja, and B. Johansson, Solid State Ionics **167**, 221 (2004).
[28] Jonas Howing, Ph.D. thesis, Acta Universitatis Upsaliensis, Uppsala, 2004.
[29] D. P. Chen, A. Maljuk, and C. T. Lin, J. Cryst. Growth **284**, 86 (2005).
[30] D. P. Chen, X. Wang, Y. S. Hu, C. T. Lin, S. X. Dou, and R. Nigam, J. Appl. Phys. **101**, 09N512 (2007).
[31] M. Mercier and J. Gareyte, Solid State Commun. **5**, 139 (1967).
[32] M. Mercier and P. Bauer, C. R. Seances Acad. Sci., Ser. B **267**, 465 (1968).
[33] M. Mercier, J. Gareyte, and E. F. Bertaut, C. R. Seances Acad. Sci., Ser. B **264**, 979 (1967).
[34] J. Li, V. O. Garlea, J. L. Zarestky, and D. Vaknin, Phys. Rev. B **73**, 024410 (2006).
[35] V. I. Formin, V. P. Gnezdilov, V. S. Kurnosov, A. V. Peschanskii, A. V. Yeremenko, H. Schmid, J.-P. Rivera, and S. Gentil, Low Temp. Phys. **28**, 203 (2002).
[36] G. M. Sheldrick, SHELXL97, University of Göttingen, Germany, 1997.
[37] C. Kittel, *Introduction to Solid State Physics*, 8th ed. (Wiley, New York, 2005), p. 449.
[38] Allan H. Morrish, *The Physical Principles of Magnetism* (Wiley, New York, 1965), pp. 447–453.
[39] A. Honma, J. Phys. Soc. Jpn. **15**, 456 (1960).
[40] M. E. Lines, Phys. Rev. **156**, 543 (1967).
[41] D. Dai, M.-H. Whangbo, H.-J. Koo, X. Rocquefelte, S. Jobic, and A. Villesuzanne, Inorg. Chem. **44**, 2407 (2005).
[42] Olivier Kahn, *Molecular Magnetism* (VCH, New York, 1993), p. 27.
[43] M. H. Jung, A. H. Lacerda, and T. Takabatake, Phys. Rev. B **65**, 132405 (2002).
[44] R. Kubo, Phys. Rev. **87**, 568 (1952).
[45] J. G. Creer and G. J. Troup, Phys. Lett. **32A**, 439 (1970).
[46] R. P. Santoro and R. E. Newman, Acta Crystallogr. **22**, 344 (1967).
[47] S. Shi, C. Ouyang, Z. Xiong, L. Liu, Z. Wang, H. Li, D. Wang, L. Chen, and X. Huang, Phys. Rev. B **71**, 144404 (2005).
[48] D. Arcon, A. Zorko, R. Dominko, and Z. Jaglicic, J. Phys.: Condens. Matter **16**, 5531 (2004).
[49] F. B. Koch and M. E. Fine, J. Appl. Phys. **38**, 1470 (1967).
[50] *Magnetism Fundamentals*, edited by E. Du Tremolet de Lacheisserie, D. Gignoux and M. Schlenker (Springer, New York,

2005), p. 266.
[51] J. L. Horwood, M. G. Townsend, and A. H. Webster, J. Solid State Chem. **17**, 35 (1976).
[52] E. Gurewitz, J. Makovsky, and H. Shaked, Phys. Rev. B **9**, 1071 (1974).
[53] M. Wakeshima, K. Ino, and Y. Hinatsu, Solid State Commun. **120**, 145 (2001).
[54] *Magnetism—Fundamentals*, edited by D. Gignoux and M. Schlenker (Springer, New York, 2005), p. 122.
[55] T. E. Westre, P. Kennepohl, J. G. DeWitt, B. Hedman, K. O. Hodgson, and E. I. Solomon, J. Am. Chem. Soc. **119**, 6297 (1997).
[56] O. Haas, A. Deb, E. J. Cairns, and A. Wokaun, J. Electrochem. Soc. **152**, A191 (2005).
[57] M. Giorgetti, M. Berrettoni, S. Scaccia, and S. Passerini, Inorg. Chem. **45**, 2750 (2006).
[58] A Deb, U. Bergmann, E. J. Cairns, and S. P. Cramer, J. Phys. Chem. B **108**, 7046 (2004).
[59] A. Hunt, W.-Y. Ching, Y.-M. Chiang, and A. Moewes, Phys. Rev. B **73**, 205120 (2006).
[60] A. Augustsson, G. V. Zhuang, S. M. Butorin, J. M. Osorio-Guillén, C. L. Dong, R. Ahuja, C. L. Chang, P. N. Ross, J. Nordgren, and J.-H. Guo, J. Chem. Phys. **123**, 184717 (2005).
[61] M. Abbate, S. M. Lala, L. A. Montoro, and J. M. Rosolen, Electrochem. Solid-State Lett. **8**, A288 (2005).
[62] A. Yamada, Y. Kudo, and K. Liu, J. Electrochem. Soc. **148**, A747 (2001).
[63] G. Liang, Y. Guo, D. Badresingh, W. Xu, Y. Tang, M. Croft, J. Chen, A. Sahiner, Beom-hoan O, and J. T. Markert, Phys. Rev. B **51**, 1258 (1995).
[64] G. Liang, A. Sahiner, M. Croft, W. Xu, X.-D. Xiang, D. Badresingh, W. Li, J. Chen, J. Peng, A. Zettl, and F. Lu, Phys. Rev. B **47**, 1029 (1993).
[65] A. Sahiner, M. Croft, S. Guha, I. Perez, Z. Zhang, M. Greenblatt, P. A. Metcalf, H. Jahns, and G. Liang, Phys. Rev. B **51**, 5879 (1995).
[66] A. Sahiner, M. Croft, Z. Zhang, M. Greenblatt, I. Perez, P. Metcalf, H. Jhans, G. Liang, and Y. Jeon, Phys. Rev. B **53**, 9745 (1996).
[67] J. J. Lagowski, *Modern Inorganic Chemistry* (Dekker, New York, 1973), pp. 695–699.
[68] B. N. Figgis and M. A. Hitchman, *Ligand Field Theory and Its Applications* (Wiley-VCH, New York, 2000), p. 10.
[69] C. Brouder, J. Phys.: Condens. Matter **2**, 701 (1990).
[70] Eugen Merzbacher, *Quantum Mechnics*, 3rd ed. (Wiley, New York, 1998), Chap. 19.
[71] S. Bocharov, Th. Kirchner, G. Dräger, O. Šipr, and A. Šimunek, Phys. Rev. B **63**, 045104 (2001).